Electronic Supplementary Material (ESI) for Soft Matter

Supporting Information for
Harnessing instabilities for design of soft reconfigurable auxetic/chiral materials

Jongmin Shim,[1,2] Sicong Shan,[3,2] Andrej Košmrlj,[4] Sung H. Kang,[3]
Elizabeth R. Chen,[3] James C. Weaver,[5] and Katia Bertoldi[3,6]

[1] *Department of Civil, Structural and Environmental Engineering, University at Buffalo, NY, 14260, USA*
[2] *J.S. and S.S. contributed equally to this work*
[3] *School of Engineering and Applied Sciences, Harvard University, Cambridge, Massachusetts 02138, USA*
[4] *Department of Physics, Harvard University, Cambridge, Massachusetts 02138, USA*
[5] *Wyss Institute for Biologically Inspired Engineering, Harvard University, Cambridge, Massachusetts 02138, USA*
[6] *Kavli Institute, Harvard University, Cambridge, Massachusetts 02138, USA*

ANALYSIS - DESIGN PRINCIPLES

From tilings of the 2D Euclidean plane to porous structures

To identify possible periodic monodisperse circular hole arrangements in elastic plates where buckling can be exploited as a mechanism to reversibly switch between undeformed/expanded and deformed/compact configurations, we investigate the hole arrangements by considering geometric constraints on the tilings (i.e., tessellations) of the 2D Euclidean plane.

In order for all the monodisperse circular holes to close through buckling of the ligaments, the plates should meet the following requirements: (a) the center-to-center distances of adjacent holes are identical, so that all the ligaments are characterized by the same minimum width and undergo the first buckling mode in an approximately uniform manner; (b) there is an even number of ligaments around every hole, so that the deformation induced by buckling leads to their closure. Mathematically, these geometric constraints can be rephrased as: the skeleton of the porous structure should (a') be a convex uniform tiling of the 2D Euclidean plane (which are vertex-transitive and have only regular faces) (b') with an even number of faces meeting at each vertex. Focusing on 1-uniform tilings (i.e. Archimedean tilings) where all the vertices are the same, so that all the holes deform similarly, we find that there are only four tessellations which meet the above requirements: *square tiling*, *triangular tiling*, *trihexagonal tiling* and *rhombitrihexagonal tiling* (see Fig. S1-A). The corresponding porous structures are then obtained by placing a circular hole at each vertex of the four tilings (see Fig. S1-B). Finally, we note that each periodic porous structure has an underlying kinematic model which comprises of a network of rigid polygons and hinges (see Fig. S1-C). These kinematic models can be obtained by transforming the circular holes either to (*i*) squares, if they are surrounded by four thin ligaments (as in the cases of 4.4.4.4, 3.6.3.6, 3.4.6.4); or (*ii*) hexagons, if they are surrounded by six thin ligaments (as in the cases of 3.3.3.3.3.3).

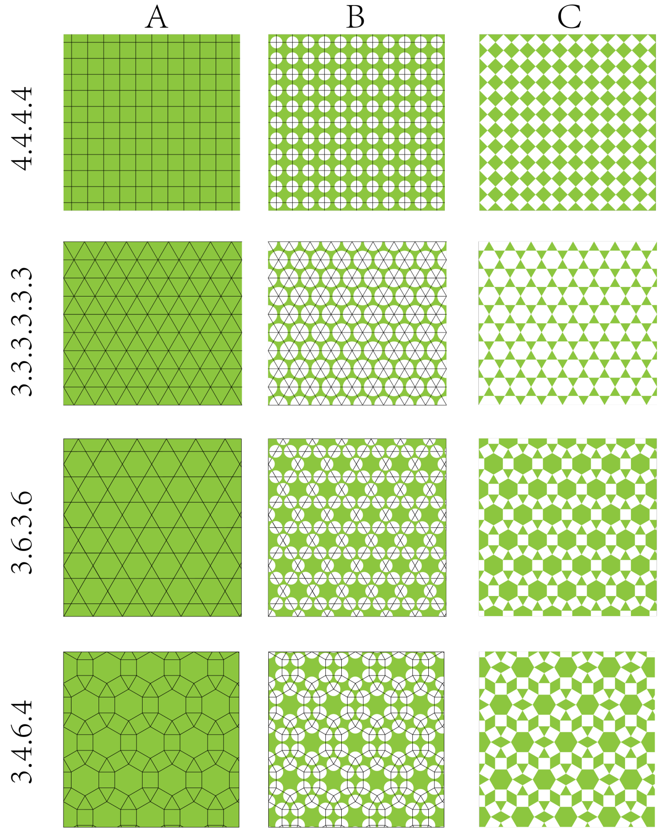

Figure S1: From tilings to porous structures. (A) We start with a solid sheet of material and draw a tiling pattern on the sheet. (B) The corresponding porous structure is then obtained by placing a circular hole at each vertex of the tiling. (C) The corresponding kinematic model can be obtained by transforming the circular holes either to squares or hexagons.

The kinematic models can then be used to study the deformation mechanism of the corresponding porous structures. Fig. S2 shows the folding mechanism of the four kinematic models investigated in this study.

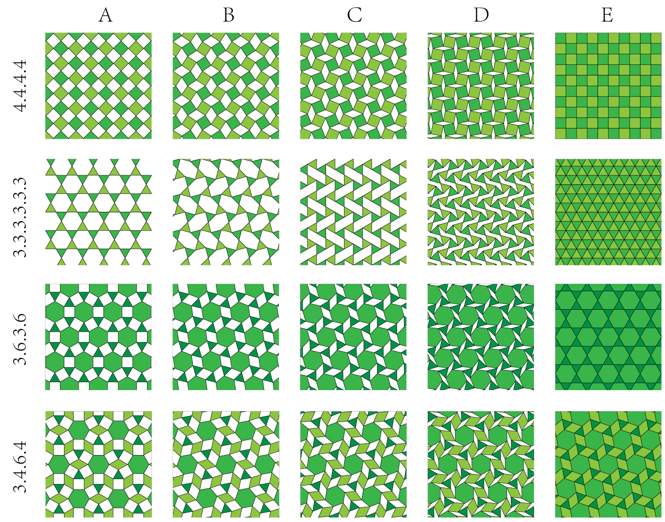

Figure S2: Folding mechanism of the kinematic models. (A) completely unfolded configuration; (B),(C) and (D) intermediate configurations; (E) completely compact/folded configuration. The polygons are colored differently only for visualization purposes.

DISLOCATION DIPOLE MODEL

It has been recently shown that the patterns induced by buckling in periodic porous structures can be investigated by making use of continuum elasticity theory and approximating the deformed holes as elastic dipoles [1]. The stress fields due to elastic dipoles are long ranged and dipoles interact with each other with interaction energy [1]

$$U_{\text{int}} = -\frac{E}{\pi}\frac{b^2 d_1 d_2}{R^2}\left[\cos\left(\theta_1+\theta_2\right)\sin\theta_1\sin\theta_2+\frac{1}{4}\right], \qquad \text{(S1)}$$

where E is the 2-dimensional Young's modulus of bulk elastic medium, R is distance between two dipoles, d_1 and d_2 are magnitudes of dipole vectors, and θ_1 and θ_2 are dipole orientations (Fig. S3A). We note that individual elastic dipoles also feel the effect of the external uniaxial compression [1], but this contribution is neglected in this study. Assuming periodic boundary conditions and independent orientations of dipoles inside the primitive cell (Fig. S6), we minimized the interaction energy of elastic dipoles (S1). For each dipole, we included interactions with $\sim$ 100 nearest dipole neighbors. The patterns that correspond to the minimized interaction energy of elastic dipoles in the four arrangements investigated in this study are shown in Fig. S3. The patterns closely resemble the patterns obtained with FE analysis (see Fig. 1-C).

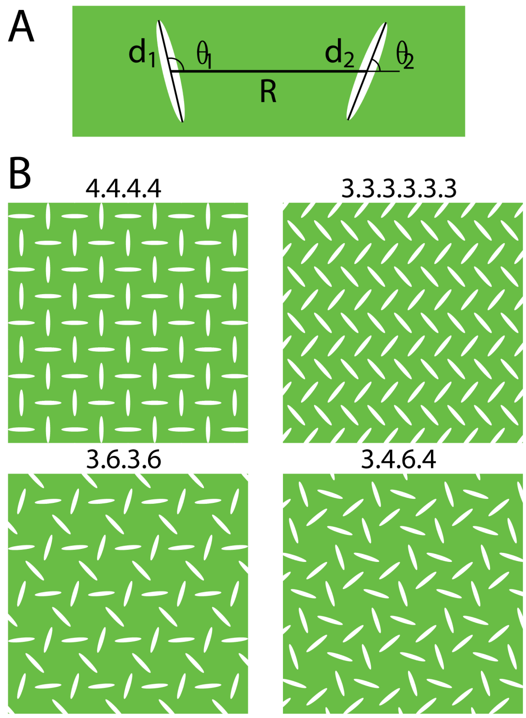

Figure S3: (A) Diagram of the interaction between two elastic dipoles (d_1 and d_2) separated by R. (B) Patterns that correspond to the minimum free energy of interactions between elastic dipoles for the four structures considered in this study.

EXPERIMENTS

Material

Silicone rubber (Vinylpolysiloxane: Elite Double 32, Zhermack) was used to cast the experimental specimens. The material properties were measured through tensile testing, up to a nominal strain $\epsilon = 0.82$. No hysteresis and rate dependence was found during loading and unloading. The stress-strain behavior was found to be accurately captured by a Yeoh hyperelastic model [2], whose strain energy density is

$$W_{\text{Yeoh}} = \sum_{i=1}^{3}\left[C_{i0}\left(\bar{I}_1-3\right)^i+\left(J-1\right)^{2i}/D_i\right] \qquad \text{(S2)}$$

where $\bar{I}_1 = \text{tr}\left[\text{dev}\left(\mathbf{F}^T\mathbf{F}\right)\right]$, $J = \det\left[\mathbf{F}\right]$, and $\mathbf{F}$ is the deformation gradient. Note that two of the parameters entering in Yeoh model are related to the conventional shear modulus (G_0) and bulk modulus (K_0) at zero strain as $C_{10} = G_0/2$ and $D_1 = 2/K_0$. To capture the behavior of the silicone rubber used in the experiments we used $C_{10} = 154\ kPa$, $C_{20} = 0\ kPa$, $C_{30} = 3.5\ kPa$, and $D_1 = D_2 = D_3 = 38.2\ GPa^{-1}$.

Specimens fabrication

The molds to cast the specimens were fabricated using a 3-D printer (Connex 500, Objet Ltd.) having a resolution of 600 *dpi* and a claimed printing accuracy of 30 μm. A very thin layer of mold release oil (Ease Release 200, Smooth-on Inc.) was sprayed onto the mold prior to molding. Then, the silicone rubber was cast into the mold. The casted mixture was first allowed to set in a vacuum for 10 minutes and then was placed at room temperature until curing was completed. The overall sizes of the four specimens are $W(\text{width}) \times H(\text{height}) \times T(\text{thickness}) = 80.0 \times 80.0 \times 35.0 mm, 86.6 \times 75.0 \times 35.0 mm, 93.3 \times 97.0\ mm \times 35.0\ mm$ and $132.0 \times 137.1\ mm \times 55.0\ mm$ for 4.4.4.4, 3.3.3.3.3.3, 3.6.3.6, 3.4.6.4, respectively. Note that large out-of-plane thicknesses were employed for all the specimens in order to avoid out-of-plane buckling modes during the uniaxial compression tests. The four samples were designed to have a void-volume-fraction $\psi = 0.50$ and holes with radius $r = 4.0\ mm$. This resulted in a center-to-center distance between adjacent holes of $a = 10.8\ mm$ for the 3.3.3.3.3.3 pattern, $a = 9.3\ mm$ for the 3.6.3.6 pattern, and $a = 9.7\ mm$ for the 3.4.6.4 pattern. Note that the fabricated samples were found to have a slightly lower void-volume-fraction (i.e. $\psi_{4.4.4.4} = 0.49$, $\psi_{3.3.3.3.3.3} = 0.48$, $\psi_{3.6.3.6} = 0.49$, $\psi_{3.4.6.4} = 0.49$), due to the limited accuracy of the 3D printer. This deviation has been accounted for in the simulations.

Testing

Uniaxial compressive experiments were performed on a standard quasi-static loading frame (Instron 5566) with a 10 kN load cell (Instron 2710-106) in a displacement-controlled manner. The specimens were compressed within flat compression fixtures. Note that the specimen was not clamped to the fixtures, but friction between the specimen and fixture surface was enough to hold the position of the specimens' top and bottom faces because no lubricant was used on the horizontal surfaces. The compression tests were performed at the cross-head velocity of 20 mm/min until the holes were almost closed. During the test, a Nikon D90 SLR camera facing the specimen was used to take pictures at every nominal strain increment of $\Delta\epsilon = 0.006$. The specimens were marked with black dots, so that we were able to quantify the changes in the geometry of the structures induced by deformation with a post-processing code in MATLAB.

Calculation of $\bar{\epsilon}_{xx}$, $\bar{\epsilon}_{yy}$, $\bar{\nu}$ and , $\bar{\nu}_{inc}$ from experiments

To quantify the lateral contraction (and thus the negative Poisson's ratio) of the porous structures in experiments, we investigated the evolution of the microstructure. The physical samples were marked with black dots as shown in Fig. 2 in the main text and their position was recorded using a high-resolution digital camera and then analyzed by digital image processing (MATLAB). All the black markers were identified in the initial frame (Fig. S4-A), and followed through the loading process. We only focused on the central part of the samples where the response was clearly more uniform and marginally affected by the boundary conditions. We first constructed several parallelograms connecting the markers in the central part of the sample (Fig. S4-B) and monitored their evolution as a function of the applied deformation. All the markers and their corresponding parallelograms which were used in the calculations, are highlighted in green in Fig. S4-C. For each parallelogram, local values of the engineering strain ϵ_{xx} and ϵ_{yy} were calculated from the positions of its vertices at each recorded frame t as

$$\epsilon_{xx}(t) = \frac{(x_4(t) - x_3(t)) + (x_2(t) - x_1(t))}{2 \mid \mathbf{L}_{34}^0 \mid} - 1, \quad \text{(S3)}$$

$$\epsilon_{yy}(t) = \frac{(y_1(t) - y_3(t)) + (y_2(t) - y_4(t))}{2 \mid \mathbf{L}_{13}^0 \mid \cos\theta} - 1, \quad \text{(S4)}$$

where $(x_i,\, y_i)$ denote the coordinates of the i-th vertex of the parallelogram, $\mid \mathbf{L}_{34}^0 \mid$ and $\mid \mathbf{L}_{13}^0 \mid$ are the norm of the lattice vectors spanning the parallelogram in the undeformed configuration (see Fig. 4-A in the main text) and $\theta = \arccos \frac{\mathbf{L}_{34}^0 \cdot \mathbf{L}_{13}^0}{|\mathbf{L}_{34}^0||\mathbf{L}_{13}^0|}$. The local values of the engineering strain were then used to calculate local values of the Poisson's ratio as

$$\nu(t) = -\frac{\epsilon_{xx}(t)}{\epsilon_{yy}(t)}, \quad \text{(S5)}$$

and

$$\nu_{inc}(t) = -\frac{\epsilon_{xx}(t+\Delta t) - \epsilon_{xx}(t)}{\epsilon_{yy}(t+\Delta t) - \epsilon_{yy}(t)}. \quad \text{(S6)}$$

Note that ν characterizes the lateral contraction/expansion of the structure with respect to the initial/undeformed configuration. Differently, ν_{inc} quantifies the lateral contraction/expansion with respect to the deformed configuration induced by an increment in the applied strain $\Delta\epsilon$ and allow us to describe the Poisson's ratio of a material that operates around a pre-deformed state. Finally, the ensemble averages $\bar{\epsilon}_{xx} =< \epsilon_{xx} >$, $\bar{\epsilon}_{yy} =< \epsilon_{yy} >$, $\bar{\nu} =< \nu >$ and , $\bar{\nu}_{inc} =< \nu_{inc} >$ for the central parallelograms under consideration were computed.

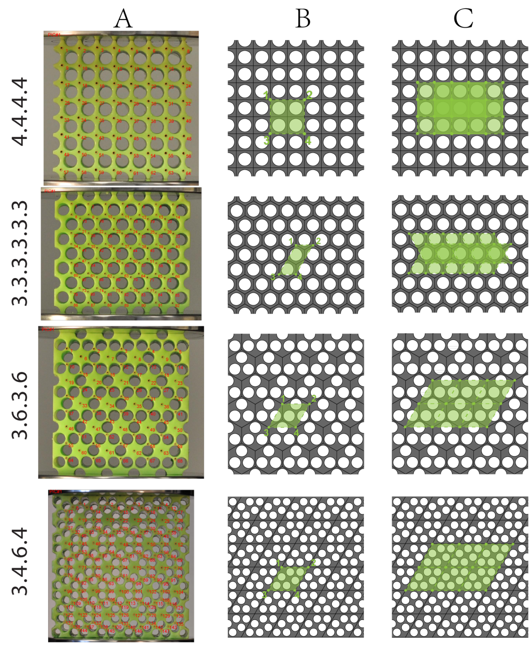

Figure S4: Illustration of calculation of $\bar{\epsilon}_{xx}$, $\bar{\epsilon}_{yy}$, $\bar{\nu}$ and $\bar{\nu}_{inc}$ from experiments. (A) The samples were marked with black dots. These markers were identified with a tracking number in the initial frame and followed through the loading process. (B) Parallelograms connecting four markers in the central part of the sample were constructed and their evolution was monitored as a function of the applied deformation. (C)All the parallelograms used in the calculations are highlighted in green.

FINITE-ELEMENT SIMULATIONS

Load-displacement analysis

The commercial finite element (FE) code ABAQUS/Standard was used for simulating the post-buckling response of the finite-size porous structures. Assuming plane strain conditions, 2D FE models were constructed using ABAQUS element type *CPE6MH* with a mesh sweeping seed size of 0.5 *mm*.

After determining the pattern transformation (the lowest eigenmode) from a buckling analysis, an imperfection in the form of the most critical eigenmode was introduced into the mesh, scaled so that its magnitude was two orders of magnitude smaller than the hole size.

As the experiments were performed under displacement-controlled conditions, load-displacement analysis were then performed imposing vertical displacements at the top surface of the FE model, while fixing the horizontal degrees of freedom. All the degrees of freedom of the bottom surface were fixed.

Instability Analysis for Infinitely Periodic Solids

Our results demonstrate that buckling in elastic plates with carefully designed arrangement of holes may be exploited to induce either the formation of chiral patterns and/or negative Poisson's ratio. However, so far we only focused on the response of structures with $\psi \simeq 0.5$, and did not explore the effect of the void-volume-fraction ψ, which can be used to control the critical strain at buckling. Since our results clearly show that the FE simulations were able to accurately reproduce the experimental results, we investigated numerically the effect of ψ on the instability of the structured plates. For the sake of computation efficiency, we focused on infinite periodic structures, and performed all the analysis on a single unit cell using appropriate boundary conditions [3, 4]. It is well known that along the loading path periodic structures can suddenly change their periodicity due to either microscopic instability (*i.e.*, instability with wavelengths that are of the order of the size of the microstructure) or macroscopic instability (*i.e*, instability with much larger wavelengths than the size of the microstructure) [3, 4]. In the following we provide a detailed description of the numerical analysis performed to detect both microscopic and macroscopic instabilities.

Infinite periodic structures In this section, we consider infinite planar periodic solids under plane strain conditions (Fig. S5-A). The periodic solid is characterized by a unit cell spanned by the lattice vectors $\mathbf{A}_1$ and $\mathbf{A}_2$ in the undeformed configuration (Fig. S5-B) and any spatial function $V(\mathbf{X})$ must satisfy the periodic condition

$$V(\mathbf{X}+\mathbf{R}) = V(\mathbf{X}) \tag{S7}$$

where with $\mathbf{R} = p_1\mathbf{A}_1 + p_2\mathbf{A}_2$, p_1 and p_2 being integers. For later use, we also introduce the reciprocal lattice vectors (Fig. S5-C)

$$\mathbf{B}_1 = 2\pi \frac{\mathbf{A}_2 \times \mathbf{A}_3}{||\mathbf{A}_1 \times \mathbf{A}_2||}\ , \quad \mathbf{B}_2 = 2\pi \frac{\mathbf{A}_3 \times \mathbf{A}_1}{||\mathbf{A}_1 \times \mathbf{A}_2||} \tag{S8}$$

where $\mathbf{A}_3 = (\mathbf{A}_1 \times \mathbf{A}_2)/||\mathbf{A}_1 \times \mathbf{A}_2||$, so that $\mathbf{A}_i \cdot \mathbf{B}_j = 2\pi\delta_{ij}$, δ_{ij} being the Kronecker delta. Thus, the reciprocal lattice vector $\mathbf{G}$ can be expressed by $\mathbf{G} = q_1\mathbf{B}_1 + q_2\mathbf{B}_2$, q_1 and q_2 being integers. Figure S5-C illustrates the reciprocal unit spanned by the primitive reciprocal lattice vectors $\mathbf{B}_1$ and $\mathbf{B}_2$.

Incremental formulation The deformation of the unit cell is described by the deformation gradient

$$\mathbf{F} = \frac{\partial \mathbf{x}}{\partial \mathbf{x}_0}, \tag{S9}$$

mapping a point in the material from the reference position $\mathbf{x}_0$ to its current location $\mathbf{x}$. The material is assumed

Electronic Supplementary Material (ESI) for Soft Matter
This journal is © The Royal Society of Chemistry 2013

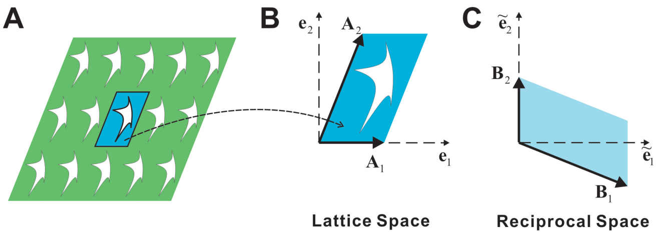

Figure S5: (A) Schematic of infinite periodic structure in two dimensional space. (B) Primitive unit spanned by the primitive lattice vectors $\mathbf{A}_1$ and $\mathbf{A}_2$. Basis vectors are denoted by $\mathbf{e}_1$ and $\mathbf{e}_2$. (C) The corresponding reciprocal unit spanned by the primitive reciprocal lattice vectors $\mathbf{B}_1$ and $\mathbf{B}_2$. Basis vectors $\tilde{\mathbf{e}}_i$ are defined by $\tilde{\mathbf{e}}_i = \frac{2\pi}{||\mathbf{A}_1\times\mathbf{A}_2||}\,\mathbf{e}_i$ for $i = 1, 2$.

to be non-linear elastic, characterized by a stored-energy function $W = W(\mathbf{F})$, which is defined in the reference configuration. The first Piola-Kirchhoff stress $\mathbf{S}$ is thus related to the deformation gradient $\mathbf{F}$ by

$$\mathbf{S} = \frac{\partial W}{\partial \mathbf{F}}. \tag{S10}$$

In the absence of body forces, the equation of motions in the reference configuration can be written as

$$\mathrm{Div}\,\mathbf{S} = \rho_0 \frac{D^2\mathbf{x}}{Dt^2}, \tag{S11}$$

where Div represents the divergence operator in the undeformed/reference configuration, D/Dt is the material time derivative and ρ_0 denotes the reference mass density.

To investigate the stability of the periodic solid, incremental deformations superimposed upon a given state of finite deformation are considered. Denoting with $\dot{\mathbf{S}}$ the increment of the first Piola-Kirchhoff stress, the incremental forms of the governing equations is given by

$$\mathrm{Div}\,\dot{\mathbf{S}} = \rho_0 \frac{D^2\dot{\mathbf{x}}}{Dt^2}, \tag{S12}$$

where $\dot{\mathbf{x}}$ denotes the incremental displacements. Furthermore, linearization of the constitutive equation (S10) yields

$$\dot{\mathbf{S}} = \mathbb{L} : \dot{\mathbf{F}}, \quad \text{with } \mathbb{L}_{ijkl} = \frac{\partial^2 W}{\partial F_{ij}\partial F_{kl}}, \tag{S13}$$

where $\dot{\mathbf{F}}$ denotes the incremental deformation gradient, and $\mathbb{L}$ denotes incremental modulus (*i.e.* elasticity tensor).

To detect microscopic instabilities, we investigate the propagation of small-amplitude elastic waves defined by

$$\dot{\mathbf{x}}(\mathbf{X}, t) = \dot{\tilde{\mathbf{x}}}(\mathbf{X}) \exp(-i\omega t)\ , \tag{S14}$$

where ω is the angular frequency of the propagating wave, and $\dot{\tilde{\mathbf{x}}}$ denotes the magnitude of the incremental displacement. It follows from (S13) that

$$\dot{\mathbf{S}}(\mathbf{X}, t) = \dot{\tilde{\mathbf{S}}}(\mathbf{X}) \exp(-i\omega t)\ , \tag{S15}$$

so that equations (S12) become

$$\mathrm{Div}\dot{\tilde{\mathbf{S}}} = \rho_0\, \omega^2 \dot{\tilde{\mathbf{x}}}\ , \tag{S16}$$

which represent the frequency-domain wave equations.

<u>*Microscopic instabilities*</u> Although microscopic (local) buckling modes may alter the initial periodicity of the solid, they can be still detected by studying the response of a single unit cell and investigating the propagation of small-amplitude waves with arbitrary wave vector $\hat{\mathbf{K}}$ superimposed on the current state of deformation [5, 6]. While a real angular frequency ω corresponds to a propagating wave, a complex ω identifies a perturbation exponentially growing with time. Therefore, the transition between a stable and an unstable configuration is detected when the frequency vanishes (i.e. $\omega = 0$) and the new periodicity of the solid introduced by instability can be easily obtained by the corresponding wave vector.

To detect the onset of microscopic instabilities, we first deform the primitive unit cell to a certain extent and then investigate the propagation of elastic waves with different wave vector

$$\hat{\mathbf{K}} = \hat{K}_1\mathbf{B}_1 + \hat{K}_2\mathbf{B}_2, \tag{S17}$$

$\hat{K}_1$ and $\hat{K}_2$ being two real numbers. For each wave vector $\hat{\mathbf{K}}$, the angular frequency ω is determined by solving the frequency domain equation (S16). In this analysis quasi-periodic boundary conditions are applied, so that

$$\dot{\tilde{\mathbf{x}}}(\mathbf{X} + \hat{\mathbf{R}}) = \dot{\tilde{\mathbf{x}}}(\mathbf{X}) \exp(i\hat{\mathbf{K}}\cdot\hat{\mathbf{R}}), \tag{S18}$$

$\hat{\mathbf{R}}$ denoting the distance in the current configuration between each pair of nodes periodically located on the boundary. Since most commercial finite-element packages do not support the complex-valued displacements introduced by (S18), following Aberg and Gudmundson [7] we split any complex-valued spatial function $\phi(\mathbf{X})$ into a real and an imaginary part,

$$\phi(\mathbf{X}) = \phi(\mathbf{X})^{re} + i\phi(\mathbf{X})^{im}. \tag{S19}$$

The problem is then solved using two identical finite-element meshes for the unit cell, one for the real part and the other for the imaginary part, coupled by

$$\dot{\tilde{\mathbf{x}}}^{re}(\mathbf{X} + \hat{\mathbf{R}}) = \dot{\tilde{\mathbf{x}}}^{re}(\mathbf{X})\cos(\hat{\mathbf{K}}\cdot\hat{\mathbf{R}}) - \dot{\tilde{\mathbf{x}}}^{im}(\mathbf{X})\sin(\hat{\mathbf{K}}\cdot\hat{\mathbf{R}}), \tag{S20}$$

$$\dot{\tilde{\mathbf{x}}}^{im}(\mathbf{X} + \hat{\mathbf{R}}) = \dot{\tilde{\mathbf{x}}}^{re}(\mathbf{X})\sin(\hat{\mathbf{K}}\cdot\hat{\mathbf{R}}) + \dot{\tilde{\mathbf{x}}}^{im}(\mathbf{X})\cos(\hat{\mathbf{K}}\cdot\hat{\mathbf{R}}). \tag{S21}$$

A microscopic instability is detected at the first point along the loading path for which a wave vector $\hat{\mathbf{K}}_{cr} = \hat{K}_{1,cr}\mathbf{B}_1 + \hat{K}_{2,cr}\mathbf{B}_2$ exist such that the corresponding angular frequency ω is zero. The instability will result in an enlarged unit cell with $n_1 \times n_2$ primitive unit cells, where

$$n_1 = \frac{1}{\hat{K}_{1,cr}}, \quad \text{and} \quad n_2 = \frac{1}{\hat{K}_{2,cr}}. \tag{S22}$$

Electronic Supplementary Material (ESI) for Soft Matter

Macroscopic instabilities Following Geymonat et al. [5], we investigate macroscopic instabilities by detecting loss of strong ellipticity of the overall response of the periodic structure. Specifically, macroscopic instabilities may develop whenever the condition

$$(\mathbf{m}\otimes\mathbf{M}):\left[\mathbb{L}^{H}:(\mathbf{m}\otimes\mathbf{M})\right]>0\ , \qquad \text{for all} \quad \mathbf{m}\otimes\mathbf{M}\neq\mathbf{0} \tag{S23}$$

is first violated along the loading path, $\mathbb{L}^H$ denoting the homogenized incremental modulus.

In this study, 2D FE simulations on the primitive cell (see Fig. S6) are performed to detect macroscopic instabilities applying periodic boundary conditions (S7). Operationally, after determining the principal solution, the components of $\mathbb{L}^H$ are identified by subjecting the unit cells to four independent linear perturbations of the macroscopic deformation gradient [6]. Then loss of ellipticity is examined by checking condition (S23) at every $\pi/360$ radian increment.

Results Here, FE simulations are performed to compute both microscopic and macroscopic instabilities under uniaxial compression for structures characterized by a wide range of void-volume-fractions, $\psi\in(0.4,0.6)$. Note that higher levels of porosity would lead to structures characterized by very thin ligaments, making them fragile. On the other hand, for smaller values of porosity the response of the structures would be highly affected by the material nonlinearity.

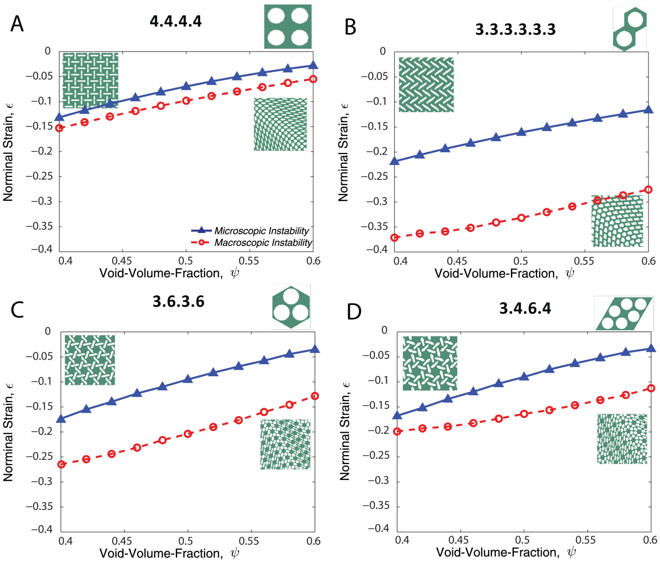

Figure S6: Nominal strain ϵ at the onset of microscopic and macroscopic instabilities as a function of the void-volume-fraction ψ. The results confirm that microscopic buckling is always critical with for the considered range of ψ.

The results of the instability analyses are summarized in Fig. S6, where the critical strain for both macroscopic and microscopic instability is reported as a function of ψ. As expected, the critical nominal strains at instability decrease for increasing values of ψ due to the reduction of the structural stiffness regardless of the types of instability. Interestingly, within the considered range of void-volume-fraction for all configurations the critical nominal strains for microscopic instability is found to be always smaller than that for macroscopic instability. Thus, these results indicate that for all configurations the folded patterns induced by microscopic buckling will emerge for a wide range of void-volume-fraction.

[1] E. A. Matsumoto and R. D. Kamien, Phys. Rev. E **80**, 021604 (2009).
[2] O. H. Yeoh, Rubber Chem. Technol. **66**, 754 (1993).
[3] N. Triantafyllidis and B. N. Maker, J. Appl. Mech. - T. ASME **52**, 794 (1985).
[4] K. Bertoldi and M. C. Boyce, Phys. Rev. B **78**, 184107 (2008).
[5] G. Geymonat, S. Muller, and N. Triantafyllidis, Arch. Ration. Mech. Anal. **122**, 231 (1993).
[6] K. Bertoldi, M. C. Boyce, S. Deschanel, S. M. Prange, and T. Mullin., J. Mech. Phys. Solids **56**, 2642 (2008).
[7] M. Åberg and P. Gudmundson, J. Acoust. Soc. Am. **102**, 2007 (1997).